

# Design of Concentric Tube Robots using Tube Patterning for Follow-the-Leader Deployment

**Cédric Girerd\***

FEMTO-ST Institute  
Univ. Bourgogne Franche-Comté/CNRS  
25000 Besançon, France  
Email: cedric.girerd@femto-st.fr

**Thomas Schlinquer**

FEMTO-ST Institute  
Univ. Bourgogne Franche-Comté/CNRS  
25000 Besançon, France  
Email: thomas.schlinquer@femto-st.fr

**Nicolas Andreff**

FEMTO-ST Institute  
Univ. Bourgogne Franche-Comté/CNRS  
25000 Besançon, France  
Email: nicolas.andreff@femto-st.fr

**Pierre Renaud**

ICube, University of Strasbourg, CNRS  
1 place de l'Hôpital  
67000 Strasbourg, France  
Email: pierre.renaud@insa-strasbourg.fr

**Kanty Rabenoroso**

FEMTO-ST Institute  
Univ. Bourgogne Franche-Comté/CNRS  
25000 Besançon, France  
Email: kanty.rabenoroso@femto-st.fr

*Concentric tube robots (CTRs) have a great potential for use in medical applications. Coupled with a follow-the-leader (FTL) deployment, they allow navigation in constrained environments. However, they are subject to instabilities if one makes use of high curvatures for the tubes, long overlapping lengths of their curved sections, or long transmission lengths. One approach to improve their stability is to pattern the tubes of which they are composed, by local removals of material along their lengths. Applying patterns on tubes was proved to be of interest for given deployed lengths of a CTR. In this paper, we present a method to enlarge the application field of CTRs that deploy in a follow-the-leader manner, by integrating tube patterning in the design process, with a stability criterion. Our method allows the designer to determine a custom pattern geometry to theoretically ensure the stability of CTRs made of any number of constant-curvature tubes, for a complete FTL deployment sequence, and while respecting a desired shape during deployment.*

## 1 Introduction

Concentric tube robots (CTRs) have been largely considered for minimally invasive medical interventions, especially for difficult-to-access organs located in confined spaces [1]. Derived from needle steering, CTRs are tele-

scopic assemblies of precurved elastic tubes usually made of Nitinol [2, 3]. The CTR backbone location is changed through rotation and translation of the individual tubes. These motions are achieved using a mechanism named the actuation unit, in which the tube bases are attached to their respective actuators. Thanks to this remote actuation, the deployed part of the CTR can achieve a very low diameter, usually about 1 mm. FTL motion was introduced by Choset and Henning [4] for serpentine robot motion planning. This kind of motion constrains the robot body to follow the path traced out by its tip. FTL motions has garnered research interest and was investigated for different robot paradigms: snake-like robots [4, 5], a binary actuated hyper-redundant robot [6], the MemoSlide based on the alternating memory method for controlling the motion of the flexible shaft [7], a magnetic extensible tendon-driven continuum robot (METABot) [8], an interlaced continuum robot with intrinsic FTL behavior [9], a soft pneumatic robot that grows from its tip [10], and CTRs [11, 12, 13]. Inspection of the olfactory cells is a good example of applied FTL motion [14]. These cells are located in the upper part of the nasal cavity, which makes the intervention site very difficult to access. Only a FTL deployment allows access to the inspection site.

The current state-of-the-art highlights three different cases to allow a FTL deployment of CTRs:  $n$  tubes with planar constant curvatures arranged in a plane,  $n$  tubes with the same helical torsion but not necessarily the same curva-

---

\*Current affiliation: Department of Mechanical and Aerospace Engineering, University of California, San Diego, La Jolla, CA 92093 USA.

tures [12], and more recently a last case where tubes have the shape of deformed helices with exponentially varying curvature magnitudes [13]. The first case is of interest for its ease of implementation and the range of applications that it addresses. Gilbert et al. [12] have introduced the study of the two-tube case for planar and helical precurvature. They have pointed out the conditions that ensure FTL deployment from the mechanics-based models of CTRs. Such deployment also requires a stable robot, with tubes that should not be subject to internal material torsion, as it may make the robot snap to configurations that do not allow a FTL deployment. The CTR stability was initially described in [15], then studied more deeply in [16, 17] and in [18] with a focus on FTL deployment.

Tube patterning is a design approach where local removal of material from the tubes modifies their bending to torsional stiffness ratio. Such structural modifications were introduced to overcome stability issues, with multi-layer helical tubes [19], patterned tubes (also called cellular tubes) with patterns defined arbitrarily [19, 20, 21] and lately defined using topology optimization approaches [22]. Their impact was evaluated theoretically and experimentally [19, 20, 21, 22], but only in the limited case of 2 tubes, and for fixed deployed lengths. Also, only trial-and-error analysis guided the pattern selection. Tube patterning has proved to enhance the stability of CTRs and eliminate the multiplicity of solutions to the kinematic model. Therefore, it is possible to get rid of the snapping phenomenon observed when several stable equilibriums are observed for the robot, and when the tubes are moving quickly from one stable equilibrium configuration to another.

Preliminary work on stable FTL deployment with a 3-tube CTR was recently presented in [14] with use of tube patterning. However, the effect of the patterning was only considered when analyzing the torsional stiffness of the tubes. This assumption does not hold, as the patterning also weakens their bending stiffnesses, thus modifying the equilibrium of the robot sections, and consequently the planar shape of the robot if the tube curvatures are not updated. To the best of our knowledge, no method exists for pattern selection during CTR design that ensures a stable FTL deployment. This paper presents such a method, by defining the patterns on each tube, while also taking into account their transmission lengths, and respecting a desired shape. The proposed

method is applicable in the case of a planar robot that follows the leader. It is possible to manage any number of constant-curvature tubes during the design, which makes the method of practical interest for CTR design.

The paper is organized as follows. Section 2 presents background information on CTR kinematics and stability criterion. A FEA-based model of tube stiffnesses is derived and analyzed in Section 3. The design method of CTRs with tube patterning is then introduced in Section 4. Each section is illustrated with the application consisting in the inspection the olfactory cells, initially considered in [14]. The conclusion of the paper is presented in Section 5.

## 2 Concentric Tube Robot Kinematics and Stability

In this section, background information on CTRs is described, along with the kinematic model and stability criterion.

### 2.1 Kinematics

In the case of planar tubes with constant curvatures, the kinematic model from [23, 24], that takes bending and torsion equilibrium of the tubes into account, is written as in Eq. (1), with  $n$  the number of tubes,  $\kappa_i$  the curvature of tube  $i$ ,  $k_{ib}$  and  $k_{it}$  its bending and torsional stiffness respectively,  $k_b = \sum_{i=1}^n k_{ib}$ ,  $\psi_i(\beta_i)$  the actuator angle,  $L_i$  its total length (see Figure 1(a)), and  $\psi_i$  its angle relative to the backbone Bishop frame (see Figure 1(b)).

$$\ddot{\psi}_i = \frac{k_{ib}}{k_b k_{it}} \sum_{j=1}^n k_{jb} \kappa_j \sin(\psi_i - \psi_j) \quad (1)$$

The boundary conditions are the tube angles at their insertion points related to their actuator angles and transmission lengths  $\psi_i(0) = \psi_i(\beta_i) - \beta_i \dot{\psi}_i(0)$ , and their derivatives with respect to the curvilinear abscissa  $s$  that are null at their free distal ends  $\dot{\psi}_i(L_i + \beta_i) = 0$ . Bishop frames are commonly used in CTR kinematics, and differ from Frenet-Serret frames in the fact that they do not experience any instantaneous rotation about their axis tangent to the curve they follow. Consequently, they don't have one of their axes laying in the local curvature plane of a curve.

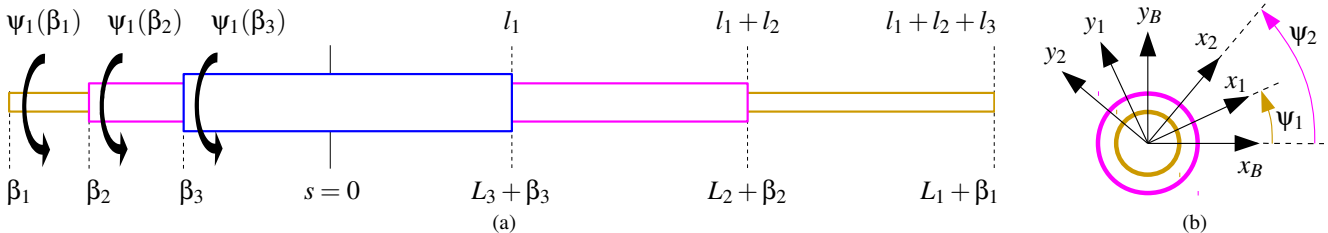


Fig. 1: (a) 3-tube CTR straightened for ease of understanding, with  $\beta_i$  the transmission length of tube  $i$ ,  $L_i$  its total length,  $\psi_i(\beta_i)$  its base angle, and (b) axial view of link 2 of the CTR with the orientation of the material base frames of tubes 1 and 2 relative to the Bishop frame.

Considering tube 1, that is present along the entire CTR body, is enough to compute the entire CTR shape. The final shape of the robot is obtained by integration of

$$\begin{cases} \dot{\mathbf{p}}_B = \mathbf{R}_B \mathbf{e}_3 \\ \dot{\mathbf{R}}_B = \mathbf{R}_B \hat{\mathbf{u}}, \end{cases} \quad (2)$$

where  $\mathbf{p}_B$  is the position of the backbone Bishop frame of the CTR that coincides with the fixed global frame at  $s = 0$ ,  $\mathbf{R}_B$  is the rotation matrix of the Bishop frame,  $\mathbf{e}_3$  is the vector of the Bishop frame which is tangent to the robot backbone, and  $\hat{\mathbf{u}}$  is the deformed curvature vector of the CTR. Eq. (2) has the associated boundary conditions  $\mathbf{p}_B(0) = \mathbf{0}$  and  $\mathbf{R}_B(0) = \mathbf{R}_z(\psi_1(0))$ .

## 2.2 Stability and FTL deployment

For a CTR made of planar constant-curvature tubes to follow the leader, a specific deployment sequence must be followed [12]. For the case of three tubes, as is considered in this paper, all three tubes first deploy together with their tips aligned, followed by the two inner tubes in the same manner, and finally the innermost tube deploys alone (see Figure 2). In this particular FTL case, a CTR made of  $n$  tubes follows a path made of  $n$  section. The robot stability can be evaluated during its deployment sequence thanks to recent works [25, 16]. They allow stability computation for CTRs made of any number of constant curvature tubes. In these approaches, Eq. (1) is linearized around an equilibrium configuration, where tubes have either aligned or opposite curvatures. Part of the result of this linearization is visible in Eq. (3), where  $\mathbf{K}_t = \text{diag}(k_{1t} \dots k_{nt})$ .

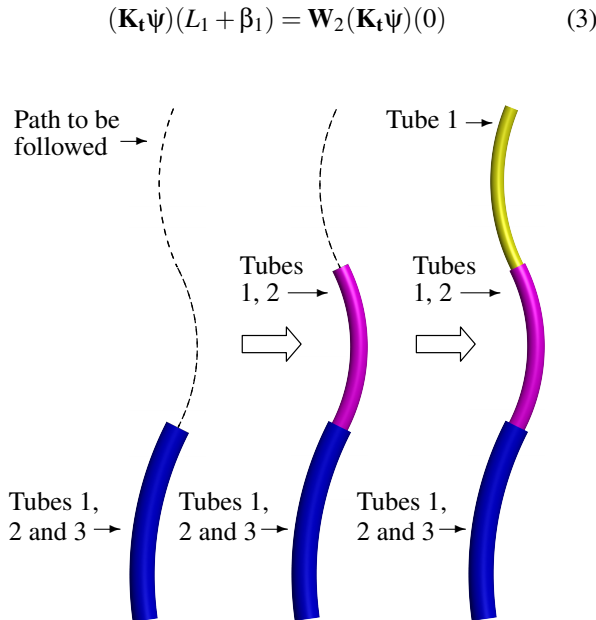


Fig. 2: FTL deployment sequence along a path to follow in the case of 3 tubes, with the three deployment steps detailed from left to right.

Tube index	1	2	3
Young's modulus (GPa)	80	80	80
Shear modulus (GPa)	30	30	30
Inner diameter (mm)	0.880	1.296	1.760
Outer diameter (mm)	1.200	1.524	2.184
Length (mm)	45.8	31.6	17.3
Bending stiffness (GPa.mm <sup>4</sup> )	5.788	10.105	51.665
Torsional stiffness (GPa.mm <sup>4</sup> )	4.352	7.598	31.846

Table 1: Characteristics of the set of tubes selected for the inspection of the olfactory cells.

$\mathbf{W}_2$  is a matrix which depends on the tube curvatures, deployed lengths, transmission lengths, bending and torsional stiffnesses. If  $|\mathbf{W}_2| < 0$ , non-trivial solutions that solve the linearized boundary value problem can be found.

For illustration purpose, the inspection of the olfactory cleft is considered in the following as it is an attractive ap-

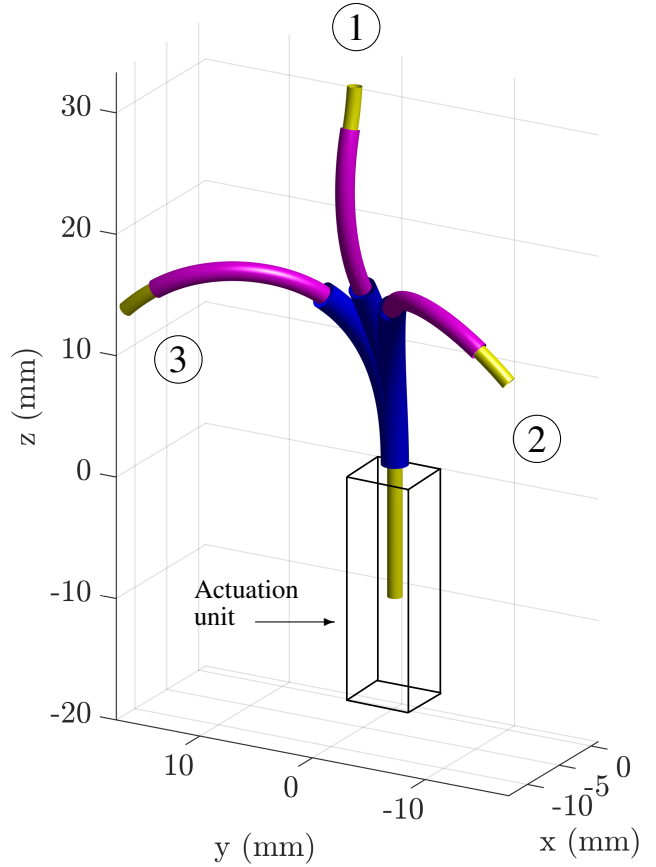


Fig. 3: Illustration of the CTR with transmission lengths, identified in [14] for the olfactory cells exploration, which is unstable in (1) and bifurcates to the stable equilibriums in (2) and (3).

plication, which requires FTL deployment [14]. The tube characteristics of the adequate CTR as identified previously are presented in Table 1. The CTR is represented during deployment in Figure 3. As illustrated, it is unstable, and thus does not fulfill the requirement  $|\mathbf{W}_2| > 0$  during deployment. In order to stabilize this robot, we are thus interested in identifying the aspect ratio of patterns that maintain  $|\mathbf{W}_2| > 0$  during the FTL deployment.

### 3 Stiffness Model of Patterned Tubes

To design the patterns of the tubes, we propose to compute their bending and torsional stiffnesses by means of finite element analysis (FEA), to be capable of assessing the impact of patterning on the stability. The pattern proposed previously in [21] is chosen for this study (see Figure 4). In [21], its aspect ratio was varied, and the corresponding values of bending and torsional stiffnesses evaluated theoretically and experimentally. More particularly, it was shown that the aspect ratio defined as  $\lambda_A = W_p/H_p$ , with  $W_p$  and  $H_p$  corresponding to the pattern width and height respectively (Figure 4) has a high impact on the values of  $\lambda$ , the ratio of the bending to the torsional stiffness of the tubes. This geometry is thus implemented and the sensitivity of  $\lambda$  to  $\lambda_A$  assessed. For our study, we choose  $n = 3$ , where  $p$  is the number of patterns for a given section of a tube that has some.

#### 3.1 Hypotheses

The modeling hypotheses are as follows: the stiffness is assessed on straight tubes, as it is classically performed [19, 20, 21, 22]. We consider the tube material to be homogeneous and isotropic, and we stay within the linear elasticity theory, hence the tube is subject only to small displacements and strains. In order to compute the bending and torsional stiffnesses from our FEA, we first ensure that our tube geometry verifies the beam theory assumptions. First, we naturally have a slender design with a high aspect ratio

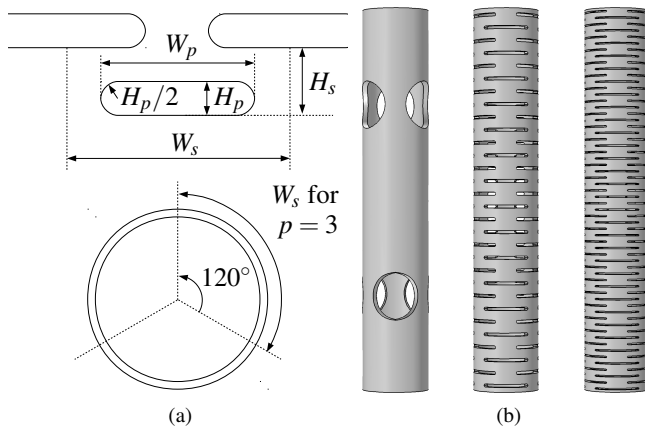


Fig. 4: (a) Parameters of the pattern adopted in this work, as presented in [21], and (b) illustration of patterned tubes with  $\lambda_A = W_p/H_p = 1, 15$  and  $30$  from left to right.

regarding length versus diameter [26]. Furthermore, to allow the use of bending and torsional stiffnesses computation formulas (Eq. (4)-(5)), following the Euler-Bernoulli beam theory is required.

$$k_b = \frac{FL^3}{3\delta} \quad (4)$$

$$k_t = \frac{TL}{\theta} \quad (5)$$

It is verified if condition of Eq. (6) is satisfied [27]:

$$\frac{EI}{KL^2AG} \ll 1, \quad (6)$$

with  $L$  the length of the beam,  $A$  its cross section area,  $E$  its elastic modulus,  $G$  its shear modulus,  $I$  the second moment of area, and  $K$  the Timoshenko shear coefficient, that depends on the geometry of the beam. In the case of a hollow circular cross section,  $K$  is given in [28] and expressed as

$$K = \frac{6(a^2 + b^2)(1 + \nu)^2}{7a^4 + 34a^2b^2 + 7b^4 + \nu(12a^4 + 48a^2b^2 + 12b^4) + \nu^2(4a^4 + 16a^2b^2 + 4b^4)}, \quad (7)$$

with  $a$  and  $b$  respectively the inner and outer radius of the tube and  $\nu$  its Poisson's ratio. For ease of comprehension, let  $\delta a$  be the wall thickness of the tube, such that  $b = a + \delta a$ . For a given tube material, Eq. (6) is thus a function of  $a$ ,  $\delta a$  and  $L$ . It is a decreasing function of  $L$ , and an increasing function of  $a$  and  $\delta a$ . For a worst case where the inner tube radius is  $a = 2$  mm, the tube wall thickness  $\delta a = 1$  mm and the tube length  $L = 20$  mm, it evaluates to 0.46, which still remains lower than 1. Thus, Eq. (4)-(5) can be used for tubes generally considered for CTRs.

#### 3.2 Finite element procedure

The FEA is implemented in COMSOL Multiphysics (COMSOL, Inc., Burlington, USA), and parameterized with  $\lambda_A = W_p/H_p$ . The ratios  $\lambda_W = W_p/W_s$  and  $\lambda_H = H_p/H_s$  are kept to the default values specified in [21], which are 0.7 and 0.25 respectively. The value of  $\lambda_A$  is then varied. Its original range is comprised between 8 and 12 in [21]. In this work, we consider a wider range comprised between 1 and 30, to potentially extend the values of  $\lambda$ , and allow to solve for a wider range of designs that have stability issues. For each aspect ratio from 1 to 30 with a step of 1, we follow the same procedure. The tube has clamped-free boundary conditions. We perform a first computation with a fixed radial

force  $F$  applied at the free end to obtain a bending displacement. As patterns are only local, the tubes do not show axis symmetry about their axis. Thus, the evaluated displacement may vary depending on the direction of application of the radial force  $F$ . A preliminary evaluation of this variation was made by changing the direction of the applied radial force  $F$ . The obtained displacements, and thus the computed bending stiffnesses, are numerically very close. Thus, the direction of application of  $F$  is chosen arbitrary. A second independent study is realized with a fixed torque  $T$  resulting in a rotation of the tube about its axis. By measuring the resulting deflection  $\delta$  and angle  $\theta$  for both studies, we can compute the bending and torsional stiffnesses,  $k_b$  and  $k_t$  respectively, using Eq. (4)-(5). They are then interpolated, and expressed as a function of  $\lambda_A$ .

### 3.3 Application

We consider the set of tubes visible in Table 1, and apply the method described above. The bending and torsional stiffnesses are computed using the FEA. A curve-fitting is made on the points of measurement for the bending and torsional stiffnesses, with the interpolant expressed in Eq. (8).

$$k_{ib}, k_{it} = \frac{p_1 \lambda_A + p_2}{\lambda_A^2 + q_1 \lambda_A + q_2} \quad (8)$$

The coefficients of the interpolant are reported in Table 2 for the three tubes. The points of measurement and the corresponding interpolant curves for the bending and torsional stiffnesses of each tube are visible in Figure 5. The values can be compared to the default values for unpatterned tubes, reported in Table 1. Figure 6 also represents the values of  $\lambda$  as a function of  $\lambda_A$ .

It is interesting to observe the range of accessible values of  $\lambda$  for the tubes, as illustrated in Figure 6. While the minimal computed value of  $\lambda$  was equal to 0.344 in the initial study [21], values as low as 0.03 are observed for high values of  $\lambda_A$ , which corresponds to patterns that have the shape of thin transverse openings. Values of  $\lambda$  higher than the de-

Coefficient	$p_1$	$p_2$	$q_1$	$q_2$
$k_{1b}$	-2.138	88.2	4.086	19.38
$k_{1t}$	2.849	425.9	0.883	212.4
$k_{2b}$	-5.471	191.7	10.2	21.31
$k_{2t}$	10.04	476.1	3.888	146.6
$k_{3b}$	-22.57	851.5	6.562	19.77
$k_{3t}$	34.71	3202	2.555	184.3

Table 2: Coefficients of the interpolant curve for the bending and torsional stiffness of tubes 1, 2 and 3, with  $k_{ib}$  and  $k_{it}$  in  $\text{GPa}\cdot\text{mm}^4$ .

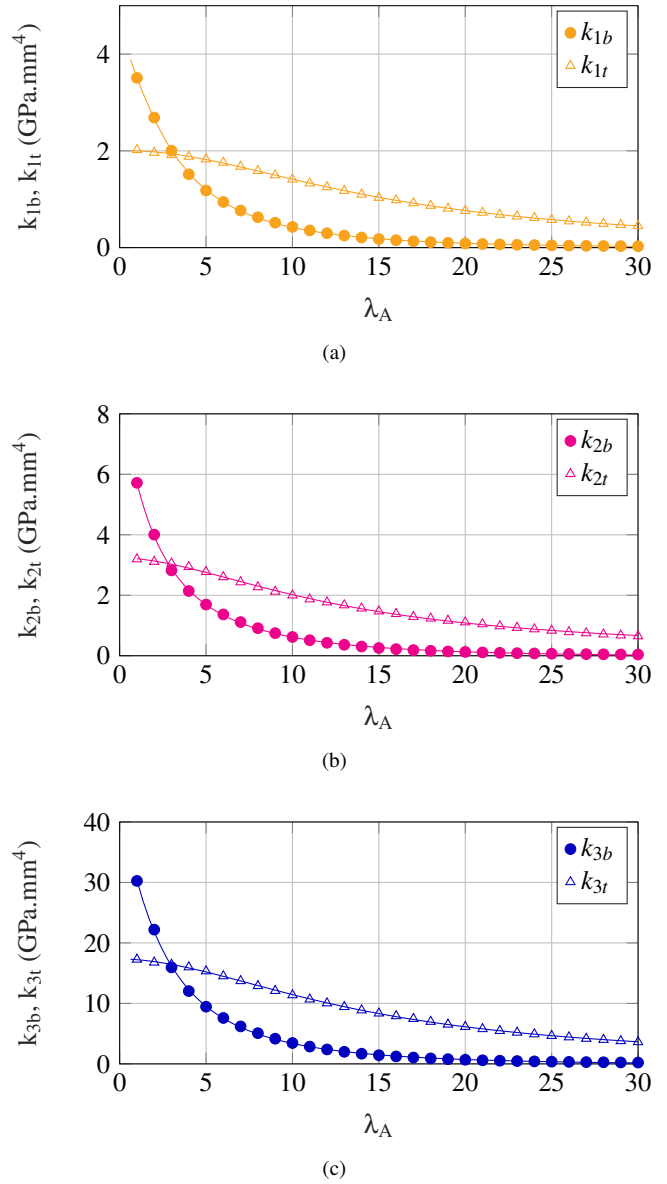


Fig. 5: Plot of the bending and torsional stiffnesses  $k_b$  and  $k_t$  with patterning for: (a) tube 1, (b) tube 2 and (c) tube 3, against  $\lambda_A$ .

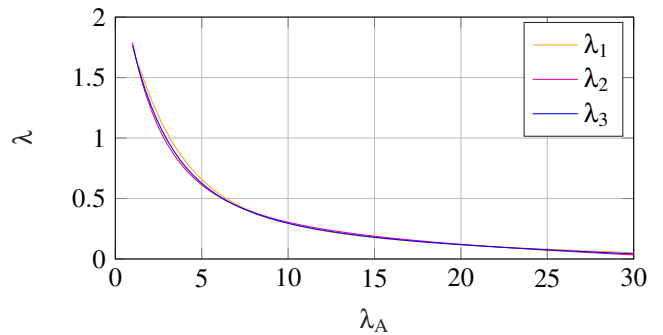


Fig. 6: Ratio of the bending to torsional stiffness for each tube as a function of  $\lambda_A$ .

fault value of 1.33 for unpatterned tubes are also observed for low values of  $\lambda_A$ , with patterns that tend to have the shape of longitudinal openings along the tubes. Indeed, extending the values of  $\lambda_A$ , originally considered between 8 and 12, to values between 1 and 30 (see corresponding pattern shapes in Figure 4 (b)), could allow to solve stability issues for a wider range of design cases. This is observed thanks to the introduction of the pattern design selection method, introduced in the following section.

## 4 CTR Design Method for FTL Deployment

### 4.1 Method

The first step of the proposed method consists in the computation of the initial tube geometries without any pattern, from the path to follow. In the case of a FTL deployment, the length  $L_i$  and curvature  $\kappa_i$  of the tubes can be determined using the curvature  $\gamma_j$ , the length  $l_j$  of the path to follow, with  $j = 1$  the index of the most proximal path segment, and  $j = n$  the most distal one [14]. Then, additional transmission lengths  $\beta_i$  can be added to each individual tube. Their values are negative as they are in the region where  $s < 0$ . As the tube synthesis is considered at full deployment of the CTR, the transmission lengths of each tube is the shortest, i.e.  $\beta_i = \beta_{imax}$ . Thus, the lengths and curvatures can be computed using Eq. (9) and Eq. (10) (see [14] for more details):

$$L_i + \beta_{imax} = \sum_{j=i}^n l_{n-j+1} \quad (9)$$

$$\kappa_1 = \gamma_1 \quad \text{and} \quad \kappa_{j,j>1} = \frac{1}{k_{ib}} \left( \sum_{i=1}^j k_{ib} \gamma_j - \sum_{i=1}^{j-1} k_{ib} \kappa_i \right) \quad (10)$$

This is illustrated in Figure 1(a). The resulting values of  $\kappa_i$  can be positive or negative depending on the direction of curvature. Therefore, the absolute value is used, and it is associated to an equilibrium angle of 0 or  $\pi$  in Eq. (11) depending on its initial sign. Thus, the vector  $\mathbf{e}$  defined by Eq. (11) can represent the equilibrium to assess.

$$e(i) = \begin{cases} 0 & \text{if } \kappa_i > 0 \\ \pi & \text{if } \kappa_i < 0 \end{cases} \quad (11)$$

Then, the robot stability is evaluated by computing  $|\mathbf{W}_2|$ . As it is a function of the deployed and transmission lengths, it is possible to compute it for the deployment sequence  $ds$  to follow. As described in Algorithm 1, the design of the robot is completed if it is stable. However, if it is not stable, the FEA of the tubes is computed, with the values of  $k_{kb}$  and  $k_{kt}$  expressed as functions of  $\lambda_A$  (Eq. (8)). Thus, the FEA is only performed one time for the synthesis of a given

tube set, and the functional approximations of the stiffnesses are then used in the main optimization loop. Initialization of our algorithm is performed by selecting  $\lambda = 1.33$ , which is the default value for Nitinol tubes. As  $\lambda$  equals the ratio of  $k_{kb}$  to  $k_{kt}$ , it allows to solve for  $\lambda_{Ak}$ , as both are a function of the latter variable. Once  $\lambda_{Ak}$  defined, the tube stiffnesses  $k_{kb}$  and  $k_{kt}$  are then computed. The new values of  $\kappa_i$  are then updated using Eq. (10), to allow the robot to have the same shape despite different bending stiffnesses. The absolute values of the tube curvatures  $\kappa_i$  are then used, and  $\mathbf{e}$  defining the tube orientations, as visible in Eq. (11).  $|\mathbf{W}_2|$  is finally computed for  $ds$  and the robot equilibrium considered  $\mathbf{e}$ , and its minimum is used to update  $\lambda$  with a step size  $\alpha$  as expressed in Eq. (12):

$$\lambda_{k+1} = \lambda_k - \alpha(\minOfDet - \min_{ds} |\mathbf{W}_2|) \quad (12)$$

---

**Algorithm 1** Pattern search algorithm for a stable CTR deployment.

---

**Input:** Path parameters  $l_j, \gamma_j, j \in [1, n]$

Tube materials and diameters

Index of tubes to pattern  $k \in [1, n]$

FTL deployment sequence  $ds$

Additional transmission lengths for the tubes  $\beta_{imax}$

Targeted value for  $\minOfDet$ , the minimum of  $|\mathbf{W}_2|$  for  $ds$

Tolerance to the targeted value  $\epsilon$

Step size  $\alpha$

**Output:**  $\lambda, \kappa_i$

1:  $k_{ib}, k_{it} \leftarrow E_i, G_i, I_i, J_i$

2:  $L_i \leftarrow$  using Eq. (9)

3:  $\kappa_i \leftarrow$  using Eq. (10)

4:  $\mathbf{e} \leftarrow$  using Eq. (11)

5:  $\kappa_i = |\kappa_i|$

6:  $|\mathbf{W}_2| \leftarrow$  using Eq. (3) for  $\mathbf{e}$  and  $ds$

7:  $error = \minOfDet - \min_{ds} |\mathbf{W}_2|$

8: **if** ( $|error| > \epsilon$ ) **then**

9:  $k_{kb}, k_{kt} = f(\lambda_{Ak}) \leftarrow$  using FEA results or expressions from an analytical model

10:  $\lambda = 1.33$

11: **while** ( $|error| > \epsilon$ ) **do**

12:  $\lambda_{Ak} \leftarrow$  using  $\lambda$  and  $k_{kb}/k_{kt}$

13:  $k_{kb}, k_{kt} \leftarrow$  using  $\lambda_{Ak}$  and Eq. (8)

14:  $\kappa_i \leftarrow$  using Eq. (10)

15:  $\mathbf{e} \leftarrow$  using Eq. (11)

16:  $\kappa_i = |\kappa_i|$

17:  $|\mathbf{W}_2| \leftarrow$  using Eq. (3) for  $\mathbf{e}$  and  $ds$

18:  $error = \minOfDet - \min_{ds} |\mathbf{W}_2|$

19:  $\lambda \leftarrow \lambda - \alpha * error$

20: **end while**

21: **end if**

22: **return**  $\lambda, \kappa_i$

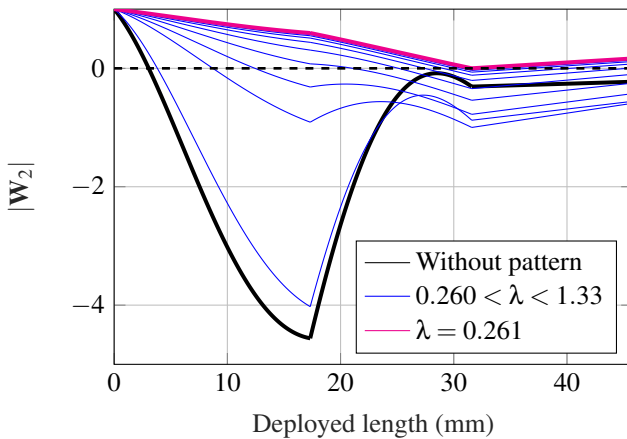
---

A value initially close to 0 can be chosen for  $\alpha$ , and then increased after trials to speed up the convergence of  $\lambda$  to its final value, while keeping the latter in the admissible range for the considered tubes (see Figure 6). In the algorithm, repetition of these steps is performed until the minimum of  $|\mathbf{W}_2|$  over  $ds$  converges to  $\text{minOfDet}$ , within a given tolerance  $\varepsilon$ . The corresponding shape of the CTR can be observed at any step of the algorithm using the kinematic model presented in Section 2. All steps of the proposed design method are summed up in Algorithm 1.

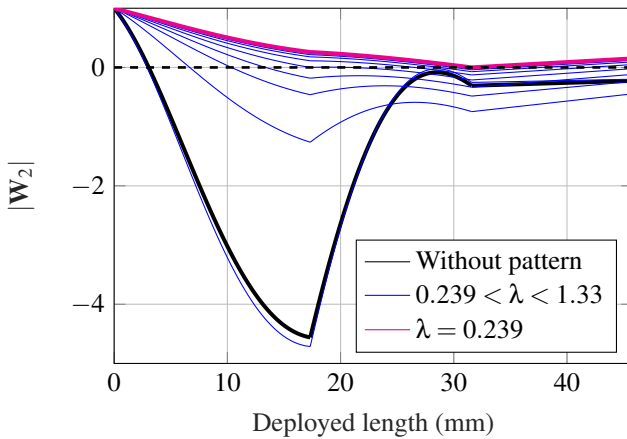
## 4.2 Application

### 4.2.1 Design with no additional transmission lengths

In this section, we consider the special case where  $\beta_{imax} = 0$ , which corresponds to no transmission lengths for the tubes after full deployment. For the 3-tube FTL deployment under evaluation, we consider the case of the structural modification of all tube combinations, with the patterning of one, two or three tubes, to explore the range of stable cases. Algorithm 1 is applied to our set of tubes. We choose for the minimum of  $|\mathbf{W}_2|$   $\text{minOfDet}$  a target value



(a)



(b)

Fig. 7: Evolution of  $|\mathbf{W}_2|$  against the deployed length of the CTR as algorithm 1 converges, in the case of the patterning of (a) tubes 1 and 2, and (b) tubes 1, 2 and 3.

	Tube 1	Tube 2	Tube 3
Patterned tubes	x	x	
$\lambda$	0.260	0.260	1.333
$\lambda_A$	11.049	11.485	-
$\kappa$ ( $\text{mm}^{-1}$ )	0.059	0.155	0.037
$k_b$ ( $\text{GPa}\cdot\text{mm}^4$ )	0.346	0.477	51.665
$k_t$ ( $\text{GPa}\cdot\text{mm}^4$ )	1.329	1.830	38.749
Patterned tubes	x	x	x
$\lambda$	0.239	0.239	0.239
$\lambda_A$	11.852	12.392	11.956
$\kappa$ ( $\text{mm}^{-1}$ )	0.059	0.156	0.065
$k_b$ ( $\text{GPa}\cdot\text{mm}^4$ )	0.302	0.411	2.412
$k_t$ ( $\text{GPa}\cdot\text{mm}^4$ )	1.265	1.724	10.109

Table 3: Stiffness ratio obtained for the combinations of patterned tubes, with the corresponding values of  $\lambda_A$ , tube curvatures and stiffnesses.

of  $1e-3$ , and  $\varepsilon = 1e-4$ , which ensures that  $|\mathbf{W}_2|$  will be positive during the entire CTR deployment. A larger margin from zero could be maintained by choosing a greater value for  $\text{minOfDet}$ . We also choose a step size  $\alpha = 0.15$ , that allows  $|\mathbf{W}_2|$  to smoothly yet quickly converge to the desired value. Stable solutions are obtained with the patterning tubes 1 and 2 after 19 iterations, and for the set of tubes 1, 2 and 3 after 18 iterations of Algorithm 1 (see animations in the video <https://cgirerd.github.io/assets/papers/girerd19jmr.mp4>). For the corresponding sets of tubes, the values of  $\lambda$ ,  $\lambda_A$ , the tube curvatures and stiffnesses, are reported in Table 3. The tube curvatures also remain in their domain of superelasticity when combined to form the robot. For each of these two cases, the curves of stability during deployment are represented in Figure 7, as  $\lambda$  converges to its final value. The obtained robot shapes, computed with the kinematic model presented in Section 2, remain perfectly in the plane during deployment with the final values computed, which validates the proposed method.

### 4.2.2 Impact of additional transmission lengths

The results presented in Section 4.2.1 are for the case where the transmission lengths of each tube equal zero at the end of the deployment. This is not realistic for physical prototypes, as tubes need to be uncovered to be seized by actuators at any time, even when fully deployed. In this case, Algorithm 1 can be followed with values of  $\beta_{imax}$  such that  $\beta_{1max} < \beta_{2max} < \beta_{3max} < 0$ . FTL deployment sequence then ensures that inequalities  $\beta_1 < \beta_2 < \beta_3 < 0$  are respected at any time during deployment [14].

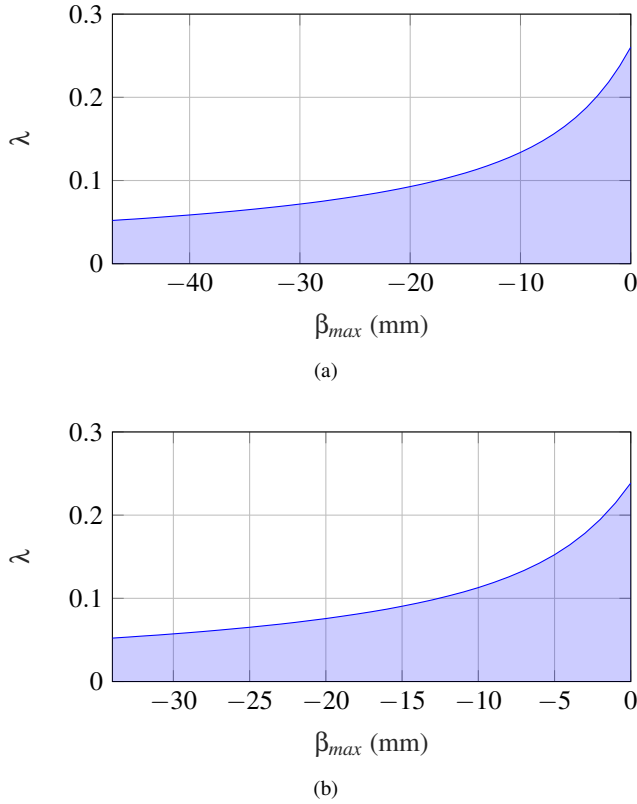


Fig. 8:  $\lambda$  as a function of  $\beta_{max}$ . Values are computed following Algorithm 1, in the case of the structural modification of (a) tubes 1 and 2, and (b) tubes 1, 2 and 3.

In this study, we propose to assess the impact of transmission lengths on the required value for  $\lambda$ , using Algorithm 1. We choose to use transmission lengths that are patterned like the deployed lengths for simplicity, to analyze the impact of additional lengths, even though unpatterned tubes and potentially other materials could be used as well [16]. The arbitrary yet realistic relationships  $\beta_{3max} = \beta_{max}$ ,  $\beta_{2max} = 2 \times \beta_{max}$  and  $\beta_{1max} = 3 \times \beta_{max}$  are introduced to constrain the problem. This also allows for the tube ends to be spread along the actuation unit, which could ease their attachment to actuators. Algorithm 1 is used to conduct the study with  $\min\text{OfDet} = 1e-3$  and  $\epsilon = 1e-4$  as in Section 4.2.1.  $\beta_{max}$  is varied with a step of 1 mm, and the value of  $\lambda$  is determined for each of them.

The curve in Figure 8 (a) represents  $\lambda$  as a function of  $\beta_{max}$  in the case of the patterning of tubes 1 and 2, and the curve in Figure 8 (b) represents  $\lambda$  as a function of  $\beta_{max}$  in the case of the patterning of tubes 1, 2 and 3. It is interesting to remark that for the range of  $\lambda_A$  considered in Section 3.2, the patterning of tubes 1 and 2 allows values of  $\beta_{max}$  as low as  $-47$  mm, while the patterning of the three tubes allows value of  $-34$  mm, corresponding to shorter transmission lengths. Thus, the patterning of tubes 1 and 2 appears as more interesting for actuation units requiring long transmission lengths. Additionally, the blue areas represent stable designs for the CTR, where using shorter transmission lengths than the ones identified when  $\min\text{OfDet} = 1e-3$

and  $\epsilon = 1e-4$  lead to a higher value for  $\min_s |\mathbf{W}_2|$  (see animations in the video <https://cgirerd.github.io/assets/papers/girerd19jmr.mp4> for a better insight on this phenomenon). Also, the tubes patterned with the values of  $\lambda$  visible on Figures 8 (a) and 8 (b) remain in their superelasticity range, which validates their synthesis.

### 4.2.3 Impact of manufacturing errors

Different manufacturing techniques have been considered up to now for the patterning of Nitinol tubes, with milling [29], laser cutting [21], electro discharge machining [30] and femtosecond laser machining [31]. Achievable accuracy varies with the process, which may result in pattern geometry errors. Accidental heat treatment of the material [31] may for instance also happen, that would modify the bending and torsional stiffness of the tubes, and thus the shape and stability of the robot.

In the case of a manufacturing process based on laser cutting of the considered pattern geometries, errors between the FEA estimation of stiffness and experimental evaluations are available [21]. For the range of tubes and patterns evaluated, the bending and torsional stiffness of the manufactured tubes were both approximately 5 to 15% lower than the ones estimated by FEA. We thus analyze the impact of such errors on the stability of the CTR with the patterning of tubes

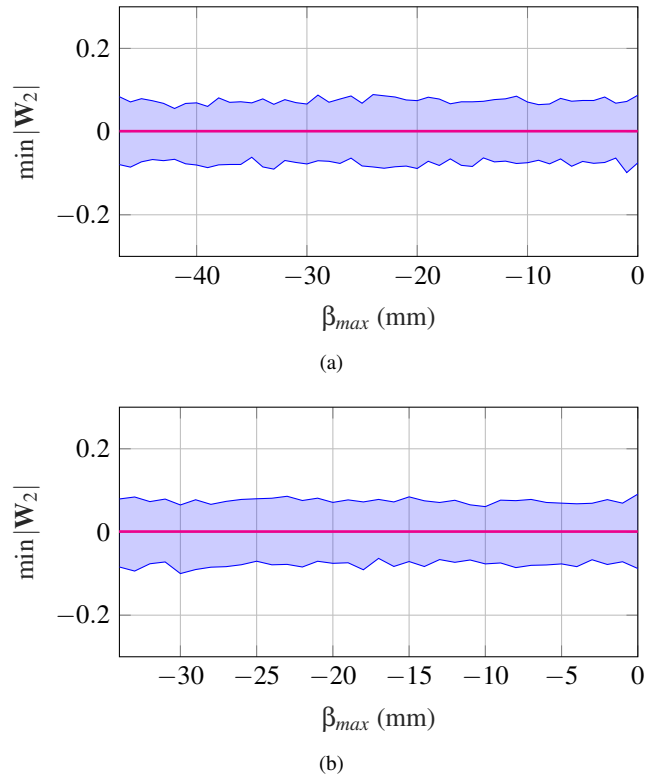


Fig. 9: Fluctuations of  $\min |\mathbf{W}_2|$  after introduction of tube stiffness errors as a function of  $\beta_{max}$  in the case of the structural modification of (a) tubes 1 and 2, and (b) tubes 1, 2 and 3. The blue areas represent the range of computed values of  $\min |\mathbf{W}_2|$ , with the targeted values in magenta.

1 and 2, and 1, 2 and 3, in the case of additional transmission lengths. We consider the bending and torsional stiffnesses errors to be independent from each other and from the pattern ratio  $\lambda_A$  as a first approximation. A random set of 100 bending and torsional stiffnesses errors are added to the one obtained in Section 4.2.2 for the patterned tubes. For each combination, new tube curvatures are computed to allow the CTR to have the desired planar shape, and their stability are then evaluated. Figure 9 represents the range of  $\min|\mathbf{W}_2|$  obtained as a function of  $\beta_{max}$ . As visible in this figure, the CTR stability varies significantly in the presence of stiffness errors, with some fluctuations around the targeted value of stability, which was set to  $1e-3$ , with a tolerance of  $\epsilon = 1e-4$ . Tube stiffness errors can either lead to stable or unstable robots, with the values of  $\min|\mathbf{W}_2|$  comprised between 0.1 and  $-0.1$ . CTR designers should thus take manufacturing uncertainties into account by adding a stability margin during the design process in Algorithm 1, depending of the manufacturing technique they use. The method adopted here can be replicated for the tubes of interest, taking into account the specific process under consideration.

## 5 Conclusions

In this paper, we have proposed a method for the design of stable CTRs with FTL deployment, that takes advantage of tube patterning. It is based on a FEA of patterned tubes, in order to determine their bending and torsional stiffnesses, and makes use of the identified models in an analytical criterion of stability. The obtained FEA results lead to a wider range of bending to torsional stiffness ratios compared to the state of the art. This shows the interest of patterning tubes with high ratios. Also, using the proposed algorithm, patterning a set of 2 or 3 tubes ensures theoretical stability of a robot with transmission lengths for the proposed application. Future work will be focused on tube patterning with different values of  $\lambda$  for the tubes, and on deepening technical development of tubes patterned with high values of  $\lambda$ , given the observed very positive impact. The impact of non-linear material behavior, tube clearance and friction in the kinematics and stability of CTRs will also be investigated, to better estimate the stability of physical prototypes.

## ACKNOWLEDGMENT

This work was supported by the French National Agency for Research within the Biomedical Innovation program (NEMRO ANR-14-CE170013), and the Investissements d'Avenir (Robotex ANR-10EQPX-44, Labex CAMI ANR-11-LABX-0004 and EUR EIPHI ANR-17-EURE-0002).

## References

- [1] Burgner-Kahrs, J., Rucker, D. C., and Choset, H., 2015. "Continuum robots for medical applications: A survey". In *IEEE Transactions on Robotics*, Vol. 31, pp. 1261–1280.
- [2] Webster, R. J., Okamura, A. M., and Cowan, N. J., 2006. "Toward active cannulas: Miniature snake-like surgical robots". In *2006 IEEE/RSJ International Conference on Intelligent Robots and Systems*, pp. 2857–2863.
- [3] Sears, P., and Dupont, P., 2006. "A steerable needle technology using curved concentric tubes". In *2006 IEEE/RSJ International Conference on Intelligent Robots and Systems*, pp. 2850–2856.
- [4] Choset, H., and Henning, W., 1970. "A follow-the-leader approach to serpentine robot motion planning". In *Journal of Aerospace Engineering*, Vol. 12.
- [5] Liljebäck, P., Pettersen, K., Stavdahl, O., and Gravidahl, J., 2012. "A review on modelling, implementation, and control of snake robots". In *Robotics and Autonomous Systems*, Vol. 60, pp. 29–40.
- [6] Tappe, S., Pohlmann, J., Kotlarski, J., and Ortmaier, T., 2015. "Towards a follow-the-leader control for a binary actuated hyper-redundant manipulator". In *2015 IEEE/RSJ International Conference on Intelligent Robots and Systems (IROS)*, pp. 3195–3201.
- [7] Henselmans, P. W., Gottenbos, S., Smit, G., and Breedveld, P., 2017. "The memoslides: An explorative study into a novel mechanical follow-the-leader mechanism". In *Proceedings of the Institution of Mechanical Engineers, Part H: Journal of Engineering in Medicine*, Vol. 231, pp. 1213–1223.
- [8] Neumann, M., and Burgner-Kahrs, J., 2016. "Considerations for follow-the-leader motion of extensible tendon-driven continuum robots". In *2016 IEEE International Conference on Robotics and Automation (ICRA)*, pp. 917–923.
- [9] Kang, B., Kojcev, R., and Sinibaldi, E., 2016. "The first interlaced continuum robot, devised to intrinsically follow the leader". Vol. 11, Public Library of Science, pp. 1–16.
- [10] Hawkes, E. W., Blumenschein, L. H., Greer, J. D., and Okamura, A. M., 2017. "A soft robot that navigates its environment through growth". Vol. 2, *Science Robotics*.
- [11] Bergeles, C., Gosline, A. H., Vasilyev, N. V., Codd, P. J., del Nido, P. J., and Dupont, P. E., 2015. "Concentric tube robot design and optimization based on task and anatomical constraints". In *IEEE Transactions on Robotics*, Vol. 31, pp. 67–84.
- [12] Gilbert, H. B., Neimat, J., and Webster, R. J., 2015. "Concentric tube robots as steerable needles: Achieving follow-the-leader deployment". In *IEEE Transactions on Robotics*, Vol. 31, pp. 246–258.
- [13] Garriga-Casanovas, A., and Baena, F. R., 2018. "Complete follow-the-leader kinematics using concentric tube robots". In *The International Journal of Robotics Research*, Vol. 37, pp. 197–222.
- [14] Girerd, C., Rabenorosoa, K., and Renaud, P., 2017. "Combining tube design and simple kinematic strategy for follow-the-leader deployment of concentric tube robots". In *Advances in Robot Kinematics 2016*, J. Lenarcic and J.-P. Merlet, eds. Springer International

- Publishing, Grasse, France, June, ch. 10, pp. 266–290.
- [15] Dupont, P. E., Lock, J., Itkowitz, B., and Butler, E., 2010. “Design and control of concentric-tube robots”. In *IEEE Transactions on Robotics*, Vol. 26, pp. 209–225.
- [16] Gilbert, H. B., Hendrick, R. J., and III, R. J. W., 2016. “Elastic stability of concentric tube robots: A stability measure and design test”. In *IEEE Transactions on Robotics*, Vol. 32, pp. 20–35.
- [17] Ha, J., Park, F. C., and Dupont, P. E., 2016. “Elastic stability of concentric tube robots subject to external loads”. In *IEEE Transactions on Biomedical Engineering*, Vol. 63, pp. 1116–1128.
- [18] Peyron, Q., Rabenorosoa, K., Andreff, N., and Renaud, P., 2018. “A numerical framework for the stability and cardinality analysis of concentric tube robots: Introduction and application to the follow-the-leader deployment”. Vol. 132, pp. 176–192.
- [19] Azimian, H., Francis, P., Looi, T., and Drake, J., 2014. “Structurally-redesigned concentric-tube manipulators with improved stability”. In 2014 IEEE/RSJ International Conference on Intelligent Robots and Systems, pp. 2030–2035.
- [20] Kim, J., Lee, D., Kim, K., Kang, S., and Cho, K., 2014. “Toward a solution to the snapping problem in a concentric-tube continuum robot: Grooved tubes with anisotropy”. In 2014 IEEE International Conference on Robotics and Automation (ICRA), pp. 5871–5876.
- [21] Lee, D., Kim, J., Kim, J., Baek, C., Noh, G., Kim, D., Kim, K., Kang, S., and Cho, K., 2015. “Anisotropic patterning to reduce instability of concentric-tube robots”. In *IEEE Transactions on Robotics*, Vol. 31, pp. 1311–1323.
- [22] Ai Xin Jue Luo, K., Looi, T., Sabetian, S., and Drake, J., 2018. “Designing concentric tube manipulators for stability using topology optimization”. In *IEEE International Conference on Robotics and Automation (ICRA)*, IEEE, pp. 1764–1769.
- [23] Dupont, P. E., Lock, J., and Butler, E., 2009. “Torsional kinematic model for concentric tube robots”. In *IEEE International Conference on Robotics and Automation*, Vol. 2009, NIH Public Access, p. 2964.
- [24] Rucker, D. C., Webster III, R. J., Chirikjian, G. S., and Cowan, N. J., 2010. “Equilibrium conformations of concentric-tube continuum robots”. In *The International journal of robotics research*, Vol. 29, SAGE Publications Sage UK: London, England, pp. 1263–1280.
- [25] Hendrick, R. J., Gilbert, H. B., and Webster, R. J., 2015. “Designing snap-free concentric tube robots: A local bifurcation approach”. In *IEEE International Conference on Robotics and Automation (ICRA)*, IEEE, pp. 2256–2263.
- [26] W. Mahoney, A., Gilbert, H., and J. Webster, R., 2016. “A review of concentric tube robots: Modeling, control, design, planning, and sensing”. In *Encyclopedia of Medical Robotics, Minimally Invasive Surgical Robotics*, pp. 181–202.
- [27] Timoshenko, S., and N Goodier, J., 1951. “The theory of elasticity”.
- [28] Hutchinson, J., 2001. “Shear coefficients for timoshenko beam theory”. In *Journal of Applied Mechanics*, Vol. 68, American Society of Mechanical Engineers, pp. 87–92.
- [29] York, P. A., Swaney, P. J., Gilbert, H. B., and Webster, R. J., 2015. “A wrist for needle-sized surgical robots”. In 2015 IEEE International Conference on Robotics and Automation (ICRA), IEEE, pp. 1776–1781.
- [30] Devreker, A., Rosa, B., Desjardins, A., Alles, E. J., Garcia-Peraza, L. C., Maneas, E., Stoyanov, D., David, A. L., Vercauteren, T., Deprest, J., Ourselin, S., Reynaerts, D., and Poorten, E. V., 2015. “Fluidic actuation for intra-operative in situ imaging”. In 2015 IEEE/RSJ International Conference on Intelligent Robots and Systems (IROS), pp. 1415–1421.
- [31] Chitalia, Y., Wang, X., and Desai, J. P., 2018. “Design, modeling and control of a 2-dof robotic guidewire”. In 2018 IEEE International Conference on Robotics and Automation (ICRA), pp. 32–37.